



# High Removal Efficiency of Methyl Orange Dye by Pure and (Cu, N) Doped TiO<sub>2</sub>/Polyaniline Nanocomposites

Mohamed Khairy<sup>1,2,\*</sup> , Eman Mohamed Kamar<sup>1</sup>, Mohamed Yehia<sup>1,4</sup>, Emad Mohamed Masoud<sup>1,3</sup> 

<sup>1</sup> Chemistry Department, Faculty of Science, Benha University, Benha, Egypt

<sup>2</sup> Chemistry Department, Faculty of Science, Imam Mohammad Ibn Saud Islamic University, Kingdom of Saudi Arabia

<sup>3</sup> Chemistry Department, Faculty of Science, Islamic University of Madinah, Kingdom of Saudi Arabia

<sup>4</sup> EL Nasr CO. for Intermediate Chemicals, Abou-Rawash, Giza, Egypt

\* Correspondence: mohkhairy@fsc.bu.edu.eg (M.K.);

Scopus Author ID: 57211258547

Received: 6.03.2021; Revised: 10.04.2021; Accepted: 14.04.2021; Published: 26.04.2021

**Abstract:** Pure polyaniline and pure and copper, nitrogen-doped TiO<sub>2</sub>/Polyaniline nanocomposites have been successfully synthesized by in-situ oxidative of aniline in aqueous media containing pure or doped TiO<sub>2</sub> nanoparticles. The as-prepared materials were characterized by TGA, XRD, FT-IR, BET, and TEM. The samples obtained have been utilized as an adsorbent to remove methyl orange from an aqueous solution. The effect of particular significant parameters such as pH, initial dye concentration, and contact time on the elimination efficiency was examined in batch experiments. The equilibrium sorption data on Ti/PANI composite were matched into Langmuir, Freundlich, and Temkin isotherms, and their parameters were fixed of the three adsorption isotherms. It is found that the R<sup>2</sup> value of the Langmuir isotherm model was the highest, with maximum removal of 94% was obtained at a pH of 7 for an adsorbent dose of 0.1 g/100 mL. The kinetic data corresponded to several models and closely followed the pseudo-second-order model for both components. Results obtained indicate that PANI and its TiO<sub>2</sub> or (Cu or N)TiO<sub>2</sub>/polyaniline nanocomposites could be used as an effective adsorbent significantly more than the PANI powder for dye deletion from water.

**Keywords:** nanocomposites; TiO<sub>2</sub>/polyaniline; dye removal; adsorption isotherm; kinetics.

© 2021 by the authors. This article is an open-access article distributed under the terms and conditions of the Creative Commons Attribution (CC BY) license (<https://creativecommons.org/licenses/by/4.0/>).

## 1. Introduction

Nowadays, the organic dyes used in many industries, such as papers, textile, pharmaceutical, food industry dyestuffs, and plastic, represent one of the most important sources of water pollution, as a result of its non-bio degradability and its high toxicity that affects human life and living organisms [1]. The decomposition of dyes is very difficult due to their resistance to heat, light, and oxidizing agents.

There are many dyes with different chemical compositions. Azo dyes are considered one of the most important of these types due to their significant applications due to their low price, stability, and variety of colors [2]. These dyes are characterized by economic cost, high stability, and have many colors. Getting rid of many dyes from the wastewater is problematic because of their good water solubility and non-biodegradable nature. There are several chemicals, physical and biological methods for disposal of these dyes from wastewater, such as photochemical decomposition, biodegradation, adsorption, chemical oxidation, and coagulation [3-9]. Among these methods is the adsorption method, which gives excellent

results due to its high ability to remove various colored materials, ease of design, low price, and economic achievement.

In the adsorption process, many adsorbents are used to remove various dyes, such as clays [10], activated charcoal [11], polymers, some agricultural residues, and metal oxides [12]. Newly conducting polymers such as polyaniline are good materials to adsorb many dyes and heavy elements [13]. Recently, polyaniline nanocomposites with rare earth oxides are used as effective adsorbents of dyes and heavy metals due to their exceptional chemical and physical properties.

One of the most important oxides with important and different applications in dyestuffs through catalysis and adsorption is titanium oxide. The importance of titanium oxide is due to its good properties, such as its inflexibility, high thermal resistance, and good optical properties. Many titanium oxide properties are improved by many processes such as doping with metals and nonmetals and forming composites with some other oxides [14].

The current study attempts to subtract a basic methyl orange dye from water using polyaniline and polyaniline composites with titanium oxide, titanium oxide doped with nitrogen and copper. The physical properties of the prepared materials are studied. The mechanism of adsorption employing adsorption isotherms and kinetic models is studied.

## 2. Materials and Methods

### 2.1. Materials.

All chemicals were used without any purification process, and all materials were analytical grade. Titanium tetrabutoxide ( $\text{Ti}(\text{OC}_4\text{H}_9)_4$ ) (97%), copper nitrate  $\text{Cu}(\text{NO}_3)_2 \cdot 3\text{H}_2\text{O}$  (99.999%) and hydrazine hydrate (80%) supplied from Sigma-Aldrich, Co., Ltd. Absolute ethanol (99%) and methyl orange dye (MO) are supplied from Adwic.

### 2.2. Synthesis methods.

#### 2.2.1. Synthesis of nano- $\text{TiO}_2$ .

Pure titanium oxide particles were synthesized using the sol-gel method [15, 16] by taking 10 ml of titanium(IV) isopropoxide and gradually adding them to 200 ml of double distilled water with violent stirring. The precipitate formed was filtered and washed several times with water and then dried at 60 °C to form a white precipitate.

#### 2.2.2. Preparation of N/ $\text{TiO}_2$ .

Nitrogen-doped  $\text{TiO}_2$  was prepared by immersing the previously prepared nano- $\text{TiO}_2$  powder in a hydrazine hydrate at 110°C [15, 16]. The white Nano- $\text{TiO}_2$  powders were dipped in a definite amount hydrazine hydrate (80%) to prepare 100 wt% for 12 h under stirring, then the precipitate filtered and dried at 110°C in the air for 3 h. Finally, the N-doped  $\text{TiO}_2$  powders were formed and denoted as N(100)/ $\text{TiO}_2$ .

#### 2.2.3. Preparation of Cu/ $\text{TiO}_2$ .

Cu-doped  $\text{TiO}_2$  nanoparticles were synthesized using the conventional impregnation method [17, 18]. A certain amount of copper nitrate ( $\text{Cu}(\text{NO}_3)_2 \cdot 3\text{H}_2\text{O}$ ) was added to prepare 0.6 wt% to a solution containing the prepared titanium oxide dispersed in ethanol. The mixture

is well stirred to form a homogeneous paste after the impregnation process. The sample was dried at 80 °C overnight and finally calcined in air for 3 h at 500 °C.

#### 2.2.4. Preparation of polyaniline.

In-situ oxidation polymerization method was used to prepare the polyaniline as the following: 1.8 ml of aniline dissolved in 100 ml of 1M HCl aqueous solution. Then 100 ml of 0.025 M of ammonium persulphate ((NH<sub>4</sub>)<sub>2</sub>S<sub>2</sub>O<sub>8</sub>) was added into the above solution drop by drop for 2h with vigorous stirring for 4 hat temperature between 0–5°C. Then the obtained dark green precipitate was filtered. The precipitate was washed several times by 1M HCl followed by distilled water, respectively, until the filtrate became colorless. Then it was re-filtered and washed once again successively by distilled water. Then it was dried at 90 °C for 12 h. Thus, finally, polyaniline was obtained.

#### 2.2.5. Preparation of PANI nanocomposites.

The TiO<sub>2</sub>/PANI nanocomposites were synthesized by oxidative polymerization of aniline in the presence of pure TiO<sub>2</sub> nanoparticles in HCl solution. The weight of samples (wt%) doped into aniline was settled at 25wt %, individually. Regularly, 100ml of 1.8 ml of aniline in 1 M HCl containing TiO<sub>2</sub> powder was ultrasonicated for 1 h. Then 100 ml of 0.025 M of ammonium persulphate was added to the above solution under vigorous stirring for 4 h at 0–5 °C. The precipitate was filtered and washed several times with distilled water and acetone until the filtrate got to be colorless. Finally, the obtained product was dried in the oven at 90 °C for 12 h. and sieving. The resulting nanocomposite is denoted at Ti/PANI.

The other nanocomposites were prepared with the same previous procedures except for the addition of certain amounts of N(100)/TiO<sub>2</sub> and Cu(0.6)/TiO<sub>2</sub> nanoparticles to prepare 15 wt% and 5 wt%, respectively of doped TiO<sub>2</sub> to aniline solution. The obtained nanocomposites were denoted as Ti(N)/PANI and Ti(Cu)/PANI for composites with (15%)N/TiO<sub>2</sub> and (5%)Cu/TiO<sub>2</sub>.

#### 2.2. Characterization tools.

The XRD patterns were evaluated for all samples in the range of 2θ from 10° to 80° at a scan rate of 5° min<sup>-1</sup> using a Philips diffractometer 321/00 apparatus at room temperature. The XRD patterns were recorded with Cu Kα radiation (λ= 1.541 Å) at 10 mA and 36 kV. The morphologies of samples were investigated via an FEI; model Tecnai G20, Super twin, double tilt 1010, at a power of 200 kV. The FT-IR spectra were monitored by double-beam Perkin Elmer Spectrometer in the region 400-4000 cm<sup>-1</sup>. The samples were mixed with KBr (1:100) to form tablets and thus confined into the sample holder. The surface properties, namely BET surface area, mean pore radius (r), and total pore volume (V<sub>p</sub>) were evaluated via adsorption of N<sub>2</sub> gas at 77 K using a conventional volumetric apparatus; (Quantachrome NOVA Automated). BJH analysis is used to determine the pore size distribution. Thermogravimetric analysis of pure PANI and their nanocomposites was performed in static air and a temperature range of 30-800 at a heating rate of 10 K/min using Dupont 2100 Thermal Analyzer.

#### 2.3. Adsorption measurements.

The removal of methyl orange (MO) from an aqueous solution by the prepared adsorbents was performed at 25°C utilizing a batch equilibrium technique. To determine the

samples' adsorption isotherms, 100 mg of the prepared materials were added to 100 ml of the dye solution with a definite initial concentration under stirring at 25 °C and pH= 7. The initial concentration of the dye was changed in the range from 60 to 120 mg/L. A portion of the solution is taken at different times. The remaining dye concentration is recorded with Jasco V-550 UV-Vis spectrophotometer (made in Japan) at  $\lambda = 463$  nm.

Based on this data, the prepared materials' equilibrium adsorption capacity is calculated using the following eq.

$$q_e = (C_0 - C_e) \frac{V}{W} \quad (1)$$

where  $C_0$  and  $C_e$  are the initial and equilibrium concentrations of dye in solution (mg/L), respectively,  $q_e$  is the adsorption capacity at equilibrium (mg/g),  $V$  is the solution volume (L), and  $W$  is the weight of adsorbent (g). The impact of pH was examined by using dilute HCl and NaOH solutions. Langmuir, Freundlich, and Temkin adsorption isotherm models were tested. The adsorption kinetics was tested by pseudo-first-order and pseudo-second-order kinetic models. All experiments were performed twice, and averaged values were calculated, where the most extreme deviation was inside 5%.

### 3. Results and Discussion

#### 3.1. Characterization.

##### 3.1.1. Thermal stability of PANI and TiO<sub>2</sub>/PANI nanocomposite.

The thermogravimetric (TGA) analysis of PANI, Ti/PANI, Ti(Cu)/PANI, and Ti(N)/PANI nanocomposites were studied under a heating rate of 10 °C min<sup>-1</sup> and was shown in Figure 1. The results show that the degradation style of nanocomposites is almost similar to PANI.

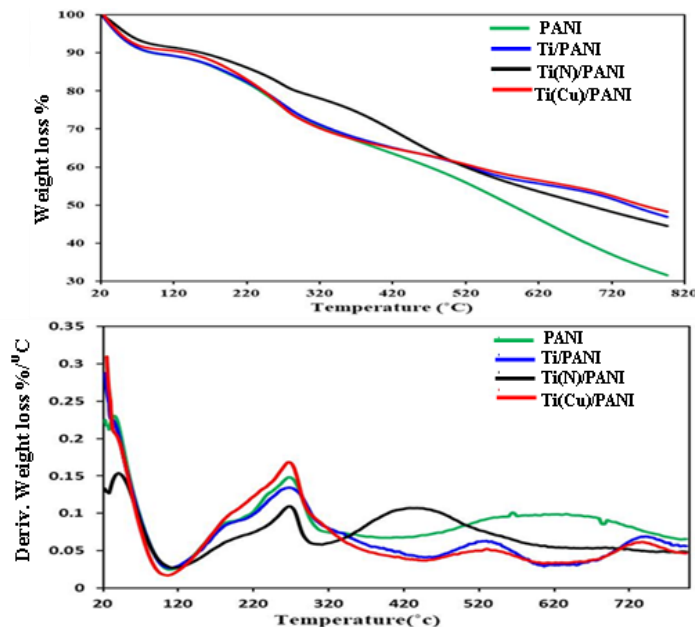


Figure 1. TGA and DTG of all investigated samples.

The TG thermogram of the pure PANI demonstrates mass loss in three stages. The first step shows a weight loss of 10.38% might be ascribed to the release of water, and the second step shows a mass loss of 21.06% might be ascribed to the release of dopant anions from PANI chains [19]. The third decomposition step starts at 400 °C and ends at 820°C with a mass loss

of 36.72%, which corresponds to the polymer's decomposition. Ti(N)/PANI nanocomposites show the same behavior as in the PANI sample. In contrast, Ti/PANI and Ti(Cu)/PANI nanocomposites show four decomposition steps. It was found that there is a decrease in the total weight loss of 68.37, 55.49, 53.10, and 50.84 for PANI, Ti(N)/PANI, Ti/PANI, and Ti(Cu)/PANI nanocomposites, respectively (Table 1). These results suggest an enhancement in the thermal stability of nanocomposites compared to PANI. This reduction in weight loss was due to a strong interaction at the interface of TiO<sub>2</sub>, N/TiO<sub>2</sub>, and Cu/TiO<sub>2</sub> and PANI, which points to the presence of nanoparticles improve the thermal stability of the conductive polymer. The results also show the highest thermal stability of Ti(Cu)/PANI nanocomposite.

**Table 1.** Thermal properties of all investigated samples.

Samples		Step (1)	Step (2)	Step (3)	Step (4)	Total loss
PANI	Wt. loss (%)	10.38	21.06	36.72	-	68.37
Ti/PANI	Wt. loss (%)	10.36	23.45	10.13	9.160	53.10
Ti(N)/PANI	Wt. loss (%)	8.326	12.78	34	-	55.49
Ti(Cu)/PANI	Wt. loss (%)	8.574	26.14	7.257	8.494	50.84

### 3.1.2. XRD.

The XRD patterns of the pure TiO<sub>2</sub>, PANI, Ti/PANI, Ti(Cu)/PANI, and Ti(N)/PANI nanocomposites are shown in Figure 2. The XRD of TiO<sub>2</sub> shows diffraction patterns of peaks for TiO<sub>2</sub> of anatase (tetragonal D4hI41/amd) structure with no evidence of the rutile phase (JCPDS files No. 21-1272 or 84-1286). The XRD pattern of PANI shows amorphous nature with some degree of crystallinity with the main diffraction peaks at about 2θ = 15.2, 21.5, and 25.3°, which is ascribed to the periodicity parallel and perpendicular to PANI chains, respectively [20].

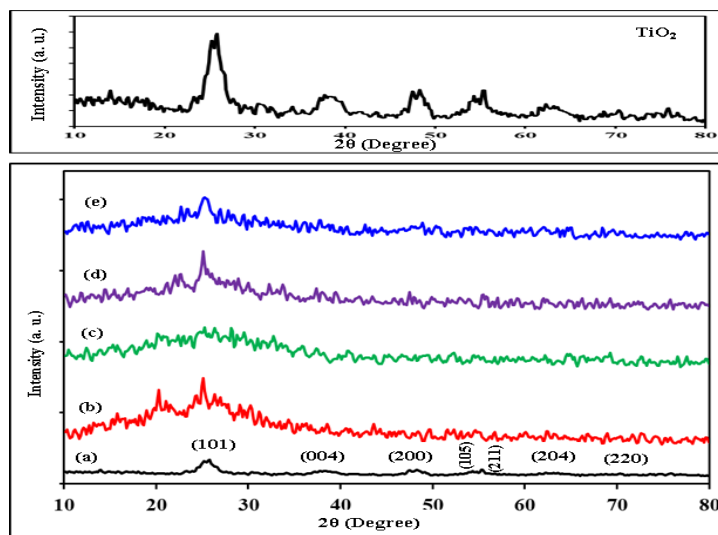


**Figure 2.** X-ray diffraction patterns of: (a) TiO<sub>2</sub>; (b) PANI; (c) Ti/PANI; (d) Ti(Cu)/PANI; (e) Ti(N)/PANI.

The XRD patterns of Ti/PANI, Ti(Cu)/PANI, and Ti(N)/PANI nanocomposites show both the characteristic peaks of TiO<sub>2</sub> and broad diffraction peaks of PANI, especially in Ti(Cu)/PANI nanocomposite. The other composites decrease the peaks related to TiO<sub>2</sub> in PANI, which suggests well dispersion of them in the PANI matrix. The prepared samples suggested having small particles due to the broad diffraction peaks of their XRD patterns. The crystallite size ( $D_{XRD}$ ) is determined from the XRD peak broadening of the most intense peak ( $2\theta=28.5^\circ$ ) using the Debye–Scherrer equation [21]. The crystallites size of the TiO<sub>2</sub> sample calculated using the Scherrer equation and is found to be 13.7 nm.

### 3.1.3. FT-IR.

The FTIR spectra of TiO<sub>2</sub>, PANI and Ti/PANI, Ti(Cu)/PANI, and Ti(N)/PANI nanocomposites specimens are given in Figure 3. The spectrum of TiO<sub>2</sub>, Figure 3a, displays bands at 419 cm<sup>-1</sup> attributed to the Ti-O-Ti framework, whereas that at 1049 cm<sup>-1</sup> is associated with Ti-O short stretching vibrations [22]. The band at 1620 cm<sup>-1</sup> is a result of the Ti-OH group [23]. These are attributed to Ti-O stretching (Table 3-A.2.3.1) ascribed to anatase structure (114) as confirmed by XRD. The spectrum shows broad bands at 3418 cm<sup>-1</sup>, which characteristic of the associated hydroxyl group that is weakly chemisorbed [24].

The FT-IR spectrum of PANI revealed a band at 3442 cm<sup>-1</sup> certified to stretching vibration of N-H groups on the polymer chain. The bands at 2924 and 2859 cm<sup>-1</sup> specifies the symmetric and asymmetric stretching vibrations of aliphatic C-H [25, 26]. The bands at 1570 are ascribed to C=C of quinonoid, and 1470 cm<sup>-1</sup> are ascribed to stretching deformation of C=C of benzenoid units of PANI [27]. The peaks observed at 1299 cm<sup>-1</sup> and 1242 cm<sup>-1</sup> corresponds to the stretching of C-N of secondary amine groups in PANI, and the band that appeared at 1116 cm<sup>-1</sup> is ascribed to C-H in-plane bending vibration. The band at 799 cm<sup>-1</sup> is assigned to C-H deformation vibration. The stretching of C-C detects around 1570 and 587 cm<sup>-1</sup> is owing to the oxidation state of polyaniline [27]. The band at 500.4 cm<sup>-1</sup> is attributed to C-N-C bonding mode of the aromatic ring. All the detected peaks were like those of pure polyaniline [28].

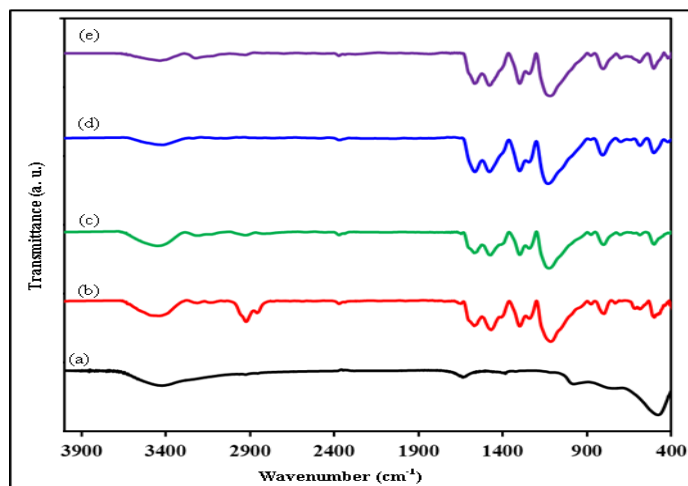


**Figure 3.** FTIR spectra of: (a) TiO<sub>2</sub>; (b) PANI; (c) Ti/PANI; (d) Ti(Cu)/PANI; (e) Ti(N)/PANI.

The spectrum of Ti/PANI nanocomposite (Figure 3c) displays bands at 3455, 1573 associated with the quinoid and benzenoid rings of polyaniline, besides peaks at 1477, 1280, 1120, 802, and 598 cm<sup>-1</sup> with a shift to a higher wavenumber compared to that of pure PANI which indicates the interaction between TiO<sub>2</sub> and PANI, Beside appearance of peaks at 480 cm<sup>-1</sup> may be related to Ti-O stretching.

The FT-IR spectrum of the Ti(Cu)/PANI nanocomposite shows a peak at 3439.4cm<sup>-1</sup> with a significant decrease in its intensity, suggesting the interaction of PANI and Cu/TiO<sub>2</sub> nanoparticles. Also, it shows peaks at 1567 and 1479.1 cm<sup>-1</sup> related to quinoid and benzenoid rings of polyaniline with some shift compared to PANI. The spectrum shows other peaks at 1299.8, 1119.5, 804.2, 589.1 cm<sup>-1</sup>. same as that observed in pure PANI with shift to higher wavenumber. Besides, the appearance of peaks at 480 cm<sup>-1</sup> may be related to Ti-O stretching.

The FT-IR spectrum of the and Ti(N)/PANI nanocomposite shows a high decrease in the intensity of peaks observed at 3417 cm<sup>-1</sup> with a significant shift to lower wavenumber than

PANI. Also, it shows the same other peaks 1564.9, 1479.1, 1299.8, 1131.1, 807.1, 586.3 and 503.3  $\text{cm}^{-1}$ .

The previous results showed that there is a connection between titanium oxide nanoparticles with the polyaniline chain. This interaction is the  $\pi$ - $\sigma$  interaction. The  $\sigma$  bond is formed by the overlap of the  $\pi$  molecular orbital of PANI with the empty d-orbital of metal ions. The  $\pi$  bond is formed by the overlap of the  $\pi^*$  molecular orbital of polyaniline with the metal's d-orbitals. Furthermore, the hydrogen bonding between the oxygen atoms on  $\text{TiO}_2$  and polyaniline chains in the composites makes  $\text{TiO}_2$  particles be inserted into the polymer chain of PANI [29].

### 3.1.4. TEM

The morphological structure was investigated by TEM, which approved the creation of nanocomposite between their components. The TEM images of PANI and Ti/PANI, Ti(Cu)/PANI, and Ti(N)/PANI nanocomposites specimens were presented in Figure 4. The TEM image of PANI (Figure 4b) displays long rods with varied sizes with length 180 nm and width 23.3 nm.

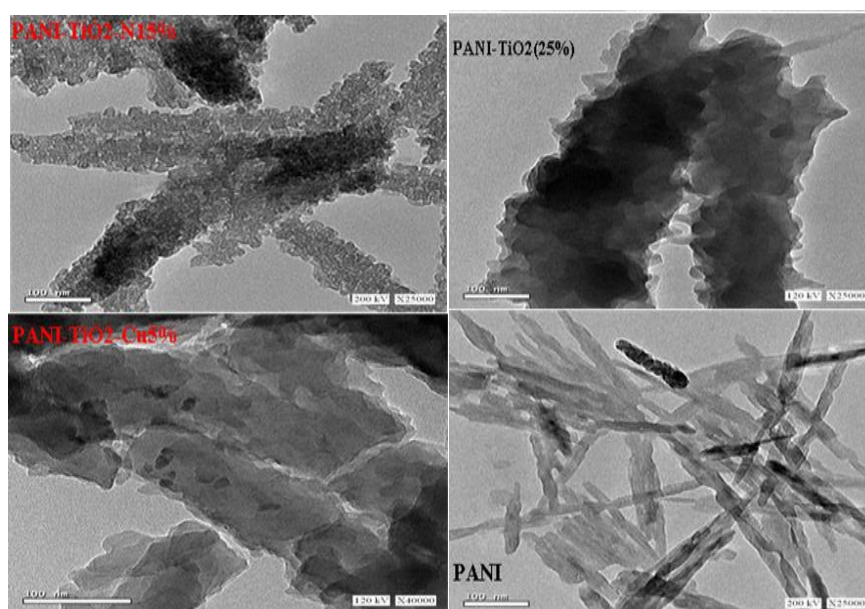


**Figure 4.** TEM images of: (a) PANI; (b) Ti/PANI; (c) Ti(Cu)/PANI; (d) Ti(N)/PANI.

Whereas, on doping with  $\text{TiO}_2$  in Ti/PANI nanocomposite, the TEM image of Ti/PANI nanocomposite demonstrates well dispersion of spherical  $\text{TiO}_2$  particles on the structure of the rod of PANI chains with particle size 20.6 nm. Figure 4c reveals the TEM image of Ti(Cu)/PANI, which shows the growth of  $\text{TiO}_2$  spherical particles on polyaniline layers with particle size 43.7 nm. TEM images of Ti(N)/PANI (Figure 4d) nanocomposites show the well distribution of  $\text{TiO}_2$  nanoparticles on the rods of polyaniline with a particle size of 17.3 nm. All samples show porous structure.

### 3.1.5. Surface properties.

Figure 5 reveals the complete adsorption isotherms of Ti/PANI, Ti(Cu)/PANI, and Ti(N)/PANI nanocomposites compared to PANI. It was observed that all samples reveal type IV with hysteresis loops of type H3, signifying mesoporous structures. The surface area of all samples was calculated using BET (Brunauer–Emmett–Teller) [30] and given in Table 2. From

Table 2, It was found that the order of increase in surface area of the samples was as follows: Ti/PANI < PANI < Ti(Cu)/PANI < Ti(N)/PANI. This might be due to the formation of the voids between the polyaniline particles due to oxide particles incorporation. All samples had total pore volumes,  $V_P$ , in the range of 0.07–0.119 ml/g. The pore radius of samples was found in the range of 6.19–16.31 nm indicating the creation of a narrow mesoporous structure, Table 2.

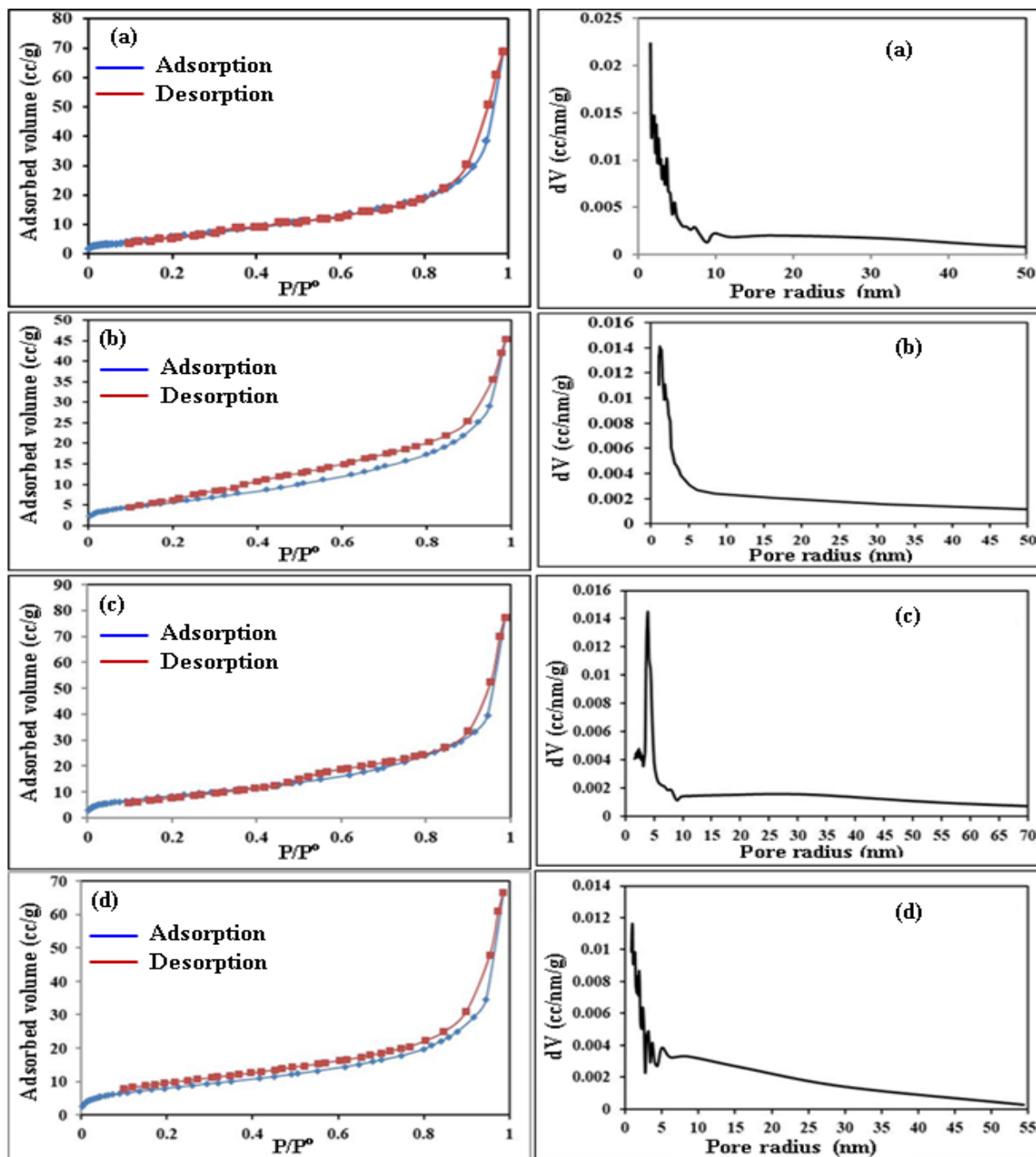


**Figure 5.** Adsorption-desorption isotherms and pore size distribution curves of: (a) PANI; (b) Ti/PANI; (c) Ti(N)/PANI; (d) Ti(Cu)/PANI.

**Table 2.** Texturing properties of all investigated samples.

Samples	$S_{BET}$ ( $m^2/g$ )	Pore volume $V_P$ (cc/g)	Pore radius (nm)
PANI	26.07	0.106	16.31
Ti/PANI	22.69	0.07	6.189
Ti(Cu)/PANI	29.57	0.103	6.961
Ti(N)/PANI	32.2	0.119	14.82



### 3.2. Adsorption parametric studies.

The adsorptive removal of methyl orange (MO) on PANI, Ti/PANI, Ti(Cu)/PANI, and Ti(N)/PANI nanocomposites from aqueous solutions was studied. Several factors affect the dye's adsorption process, such as initial dye concentration, contact time, and pH.

#### 3.2.1. Contact time effect.

Figure 6 displays the contact time effect on eliminating MO dye by each of pure PANI, Ti/PANI, Ti(Cu)/PANI, and Ti(N)/PANI nanocomposites at pH 7 and 25°C. The removal percentage (%R) of dye in the supernatant solution is calculated using the following equation:

$$\%R = \frac{C_0 - C_t}{C_0} \times 100 \quad (2)$$

where  $C_0$  (mg/L) is the dye concentration at  $t = 0$  min and  $C_t$  (mg/L) is the dye solution's concentration at time  $t$ . It was found that the adsorption process was noticeably based on the time such that most of the dye was removed in about 25 minutes. Also, under the same experimental conditions utilized, the dye uptake over the studied nanocomposites occurs faster than the pure PANI. It is remarked that as the Ti/PANI composite has the highest adsorption uptake (94.3%), this might be attributed to an excess number of adsorption sites on its surface. The elimination capabilities of dye in 20 min were ordered as: Ti/PANI > Ti(Cu)/PANI > Ti(N)/PANI > PANI > PANI. Figure 6 also shows that the dye adsorption starts fast and then decreases gradually with time. The fast beginning of adsorption is attributed to the expansive locality number of active sites on the nanocomposites' surface and the high dye concentration gradient. According to the results obtained, we concentrated our adsorption study on the Ti/PANI sample.

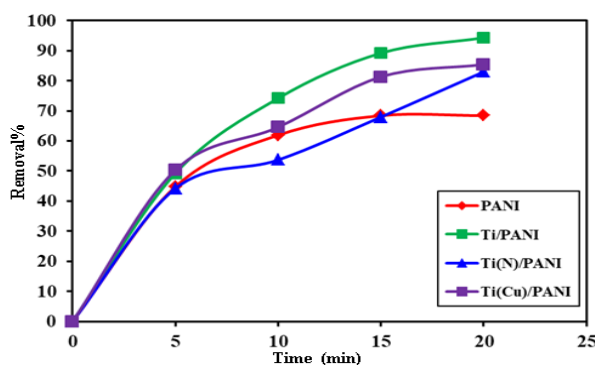


**Figure 6.** Removal% of MO dye onto PANI and their nanocomposites as a function of time. Where dye concentration is  $120 \text{ mg L}^{-1}$  and adsorbent dose is  $0.1 \text{ g}$  in  $100 \text{ mL}$ .

#### 3.2.3. effect of pH.

The adsorptive removal of MO dye was tested in the pH range 4–9 at dye concentration  $120 \text{ mg/L}$  and Ti/PANI nanocomposite concentration  $0.1 \text{ g/L}$  at  $298 \text{ K}$  and given in Figure 7.  $0.1 \text{ M HNO}_3$  or  $0.1 \text{ M NaOH}$  solution was used to adjust pH. It was found that the dye removal increases as the pH increase up to  $\text{pH} = 7$  then decreases at  $\text{pH} = 9$ . It achieves the greatest value at  $\text{pH} = 7$ . The higher values of  $q_t$  observed at acidic and neutral pH may be ascribed to the electrostatic attraction between positively charged Ti/PANI and MO anions with negative charges [31].

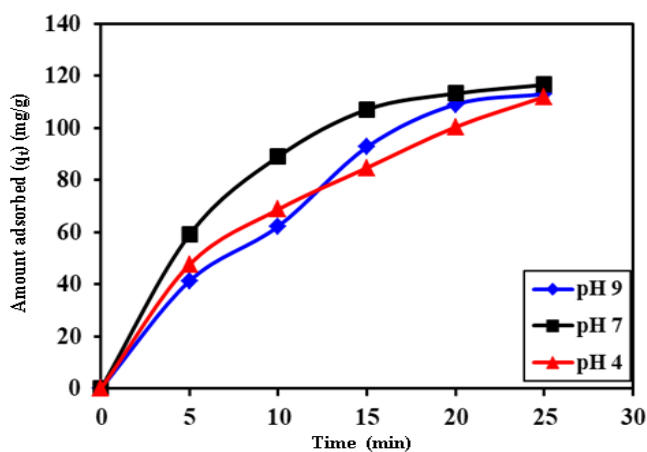


**Figure 7.** Adsorption capacity of MO dye onto Ti/PANI nanocomposite as a function of time at different pH values. Where dye concentration is 120 mg L<sup>-1</sup> and adsorbent dose is 0.1 g in 100 mL.

### 3.2.4. Effect of initial concentration of dye.

The percentage of the dye's elimination was also studied at various dye concentrations from 60 mg/L to 120 mg/L, at pH= 7 and adsorbent load = 0.1 g and given in Figure 8, as the concentration increases as the dye adsorption increases. At low concentrations, the binding sites on the adsorbent surface were accessible to all the dye molecules existing in the solution. This results in increasing the adsorption capacity. At high concentrations, the adsorption capacity was increased owing to the increasing the adsorbed dye molecules available.

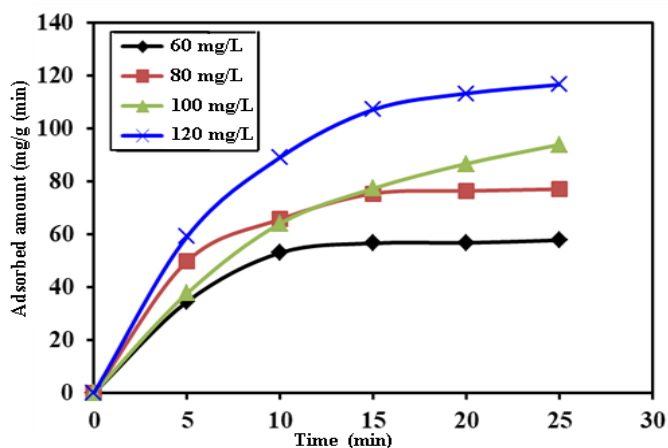


**Figure 8.** Effect of initial concentration on the adsorption capacity of MO dye onto Ti/PANI nanocomposite. The adsorbent dose is 0.1 g in 100 mL and T= 25 °C.

### 3.3. Equilibrium adsorption isotherm.

Different isotherm models can be used to analyze adsorption experimental data, such as the Langmuir, Freundlich, and Temkin models [32, 33].

Freundlich and Langmuir equations are given by Eqs. (3) and (4), respectively:

$$\ln q_e = \ln K_F + (1/n) \ln C_e \quad (3)$$

$$C_e/q_e = 1/q_{\max} K_L + 1/q_{\max} C_e \quad (4)$$

where  $q_{\max}$  is the theoretical maximum monolayer sorption capacity (mg/g),  $n$ ,  $K_F$ , and  $K_L$  are empirical constants.  $K_L$  is the Langmuir adsorption constant and evaluates the affinity of the

sorbent for the solute.  $1/n$  values reveal the isotherm type to be unfavorable ( $1/n > 1$ ), favorable ( $0 < 1/n < 1$ ) and irreversible ( $1/n = 0$ ) [34].

Whether the adsorption process is preferable or not can be determined according to the Langmuir model by  $R_L$ 's value. The value of  $R_L$  is an indicator of adsorption capability, and it can be calculated based on the following equation [35]:

$$R_L = \frac{1}{1 + K_L C_0} \quad (5)$$

where  $C_0$  is the initial dye concentration. The values of  $R_L$  show the states of isotherms to be either irreversible ( $R_L = 0$ ), unfavorable ( $R_L > 1$ ), or favorable ( $0 < R_L < 1$ ).

Temkin isotherm model was also utilized to analyze the adsorption data, and it can be given by the following equation [36]:

$$q_e = \frac{RT}{b_T} \ln A_T + \frac{RT}{b_T} \ln C_e \quad (6)$$

where  $(RT/b_T) = B$  (J/mol) is the Temkin constant related to the heat of adsorption,  $A_T$  is the equilibrium binding constant (L/g),  $b_T$  is the Temkin constant correlated to the adsorption heat (kJ/mol),  $R$  is the universal gas constant (8.314 J/mol/K), and  $T$  is the absolute temperature (K).

Freundlich, Langmuir, and Temkin models were applied to analyze the obtained experimental adsorption data on Ti/PANI nanocomposite. Figure 9 shows the relevant data of these three models.

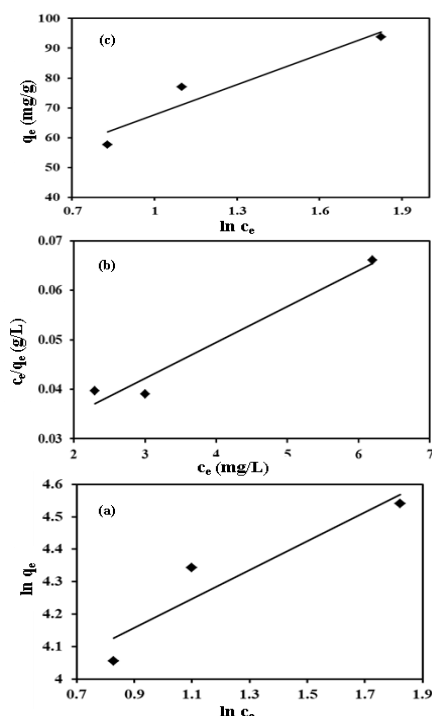


**Figure 9.** (a) Freundlich; (b) Langmuir; (c) Temkin isotherm models plots for the adsorption of MO dye on Ti/PANI, with optimum conditions: MO dye concentration (120 mg/L), amount of adsorbent= 0.1 g), contact time 20 minutes and pH = 7 and T = 298 K.

Table 3 reveals the parameters evaluated from Freundlich and Langmuir and Temkin models for the dye adsorption on Ti/PANI nanocomposite. It was observed from Table 3 the value of correlation coefficients ( $R^2$ ) of the Langmuir model is the highest one ( $R^2 = 0.963$ ) compared to the other isotherms. Accordingly, the experimental equilibrium data can be better

described by Langmuir isotherm.  $R_L$ 's value is 0.029, which is ( $0 < R_L < 1$ ), indicating that the isotherm is favorable.

**Table 3.** Langmuir, Freundlich and Temkin isotherm constants for MO dye adsorption onto Ti/PANI samples.

Model	Parameters	Adsorbents
		TiO <sub>2</sub> /PANI
Langmuir isotherm model	$q_{max}$ (mg/g)	136.9
	$q_{exp}$ (mg/g)	116.5
	$K_L$ (L/mg)	0.36
	$R^2$	0.963
	$R_L$	0.029
Freundlich isotherm model	$K_F$ (mg/g)	42.9
	$N$	2.25
	$1/n$	0.444
	$R^2$	0.873
Temkin isotherm model	$A_T$ (L/g)	2.76
	$B_T$	73.74
	$B$ (kJ/mol)	33.59
	$R^2$	0.915

### 3.4. Kinetics of adsorption.

The adsorption mechanism can be detected from the adsorption kinetics. It is known that any adsorption process takes place through three steps 1- the transfer of adsorbent molecules from the solution to the vicinity of the adsorbent, 2- Migration of adsorbent molecules from the vicinity of the adsorbent to the adsorbent surface, 3- Diffusion from the surface to the adsorption sites in the adsorbent. The slowest step in the adsorption process determines the rate of this process [37]. The pseudo-first-order [38], pseudo-second-order [39], Elovich, and intraparticle diffusion [40] models were examined to assess the mechanism of the adsorption process. A great relationship with the kinetic data clarifies the dye adsorption mechanism on the polyaniline and their nanocomposites.

Pseudo-first order is given by the following equation [38]:

$$\ln(q_e - q_t) = \ln q_e - k_1 t \tag{7}$$

where  $q_t$  and  $q_e$  are the adsorbed amounts of dye (mg/g) at time  $t$  (min) and at equilibrium, individually, and  $k_1$  ( $\text{min}^{-1}$ ) is the rate constant of pseudo-first-order. The  $\ln(q_e - q_t)$  plots versus  $t$  (Figure 10a) are used to determine the values of  $k_1$  for all specimens.

The pseudo-second-order reaction can describe the adsorption process when the reaction rate depends on the adsorbed concentration at equilibrium and the adsorbed concentration of the dye on the adsorbent surface. It is given by [39].

$$t/q_t = 1/k_2 q_e^2 + t/q_e \tag{8}$$

Figure 10b reveals the fitting plots of Equation 8 ( $(t/q_t)$  vs.  $t$ ). The values of  $q_e$ ,  $k_2$ , and  $R^2$  were estimated and recorded in Table 4.

For numerous adsorption systems, Elovich's empirical adsorption model has extensive applicability. This model was constructed based on the heterogeneity energy of adsorption sites in the form of a rectangular distribution [41]. The mathematical equation of the kinetic model of Elovich can be expressed as follows:

$$q_t = (1/\beta)\ln(\alpha\beta) + (1/\beta)\ln t \tag{9}$$

where  $\beta$  is the rate of initial adsorption of the Elovich equation ( $\text{mg.g}^{-1} \text{min}^{-1}$ ) and  $\alpha$  is the Elovich adsorption constant ( $\text{g.mg}^{-1}$ ) [42]; it is interrelated to the energy of adsorption [43]. The linear relation of the Elovich equation was obtained if  $\alpha\beta t \gg t$  and that  $q = q_t$  for a time  $t = t$  and  $q = 0$  at  $t = 0$  [44]. The values of  $\beta$  and  $\alpha$  were determined from the relation between  $q_t$  and  $\ln(t)$  (Figure 10c) and given in Table 3.

Several researchers have utilized this model to elucidate the kinetics of the adsorption of pollutants on different adsorbents. Different mechanisms such as activation of surface, its deactivation, interface phase, and diffusion in solution were explored using this model. It suffices to explain the process with greater changes in the energy of activation [45].

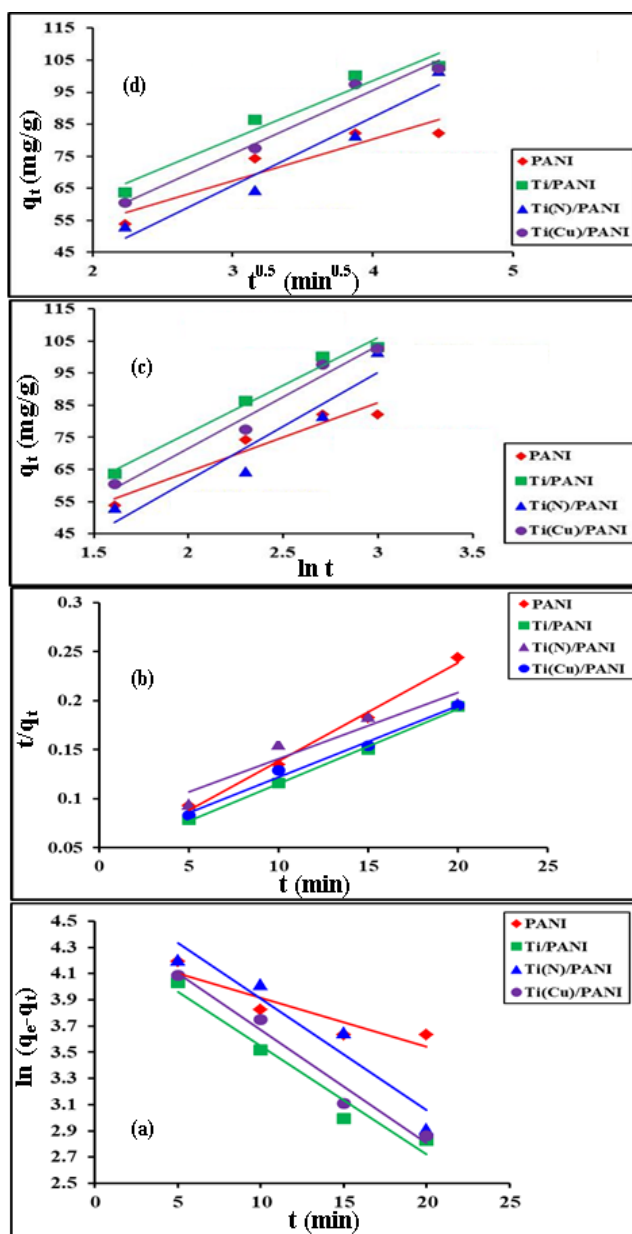


**Figure 10.** (a) Pseudo-first-order; (b) Pseudo-second-order; (c) Elovich; (d) Intraparticle diffusion models plots for the adsorption of MO dye on all samples, with optimum conditions: MO dye concentration (120 mg/L), amount of adsorbent= 0.1 g, contact time 20 minutes and pH = 7 and T = 298 K.

The results display that the pseudo-second-order kinetic model exhibited the best correlation coefficient for dye adsorption on the pure PANI, Ti/PANI, Ti(Cu)/PANI, and Ti(N)/PANI nanocomposites compared to the other models. Moreover, the obtained values of

the calculated adsorbed amount ( $q_{e, cal}$ ) are in good matching with the practical adsorbed amount values of ( $q_{e, exp}$ ), which specifies that the rate-determining step may be chemisorption.

Weber and Morris proposed an intraparticle diffusion model [37], and the adsorption data are expressed by Equation 10:

$$q_t = k_{dif}\sqrt{t} + C \tag{10}$$

where  $k_{dif}$  is the rate constant of intraparticle diffusion ( $\text{mg/gmin}^{1/2}$ ), and  $C$  is the constant correlated to the boundary layer thickness. Figure 10d shows the relation between  $q_t$  and  $t^{1/2}$ , which displays only one straight line. The values of  $k_{dif}$  and  $C$ , which are determined from the plots were listed in Table 4. The presence of only one straight line designates that only one process is involved in the process of adsorption. This process is the mass exchange of dye molecules from the mass reaction to the surface of the adsorbent.

**Table 4.** Comparison between the pseudo-first-order, pseudo-second-order, intraparticle diffusion, and Elovich models and their parameters for all investigated samples.

Models	Parameters	Adsorbents			
		PANI	Ti/PANI	Ti(N)/PANI	Ti(Cu)/PANI
Pseudo-first-order model	$q_{e,exp}$ (mg/g)	82.1	103.1	101.6	102.5
	$q_{e,cal}$ (mg/g)	72.79	79.45	116.45	92.97
	$k_1$ (L/mg)	0.037	0.083	0.085	0.086
	$R^2$	0.834	0.958	0.920	0.973
Pseudo-second-order model	$q_{e,cal}$ (mg/g)	111	119	111.1	114.9
	$k_2$ (g/(mg min))	0.0018	0.0020	0.0015	0.0019
	$R^2$	0.989	0.999	0.9589	0.9978
Intra-particle diffusion	$k_{dif}$ (mg/(g min <sup>1/2</sup> ))	13.02	19.88	21.48	19.88
	$C$	28.32	16.18	1.36	16.18
	$R^2$	0.874	0.975	0.953	0.975
Elovich model	$\beta$ (g/mg)	0.046	0.034	0.029	0.031
	$\alpha$ (mg/(g min))	0.017	0.019	0.026	0.024
	$R^2$	0.932	0.982	0.901	0.975

#### 4. Conclusions

The pure PANI, Ti/PANI, Ti(Cu)/PANI, and Ti(N)/PANI nanocomposites were synthesized via in-situ polymerization of aniline in the absence and presence of pure and doped TiO<sub>2</sub>. The adsorptive and surface properties of PANI were improved by incorporating pure or doped TiO<sub>2</sub> into the polymeric structure. The results show enhancement in the thermal stability of nanocomposites compared to PANI. The dye's removal is reached to a maximum value at pH 7 and increases with increasing contact time. The Adsorption efficiency of samples increases in the following order: Ti/PANI>Ti(Cu)/PANI > Ti(N)/PANI >PANI. The pseudo-second-order kinetic model was found to be fitted to the adsorption data of all samples. The Langmuir isotherm model was the best model for describing the equilibrium data. This study suggests that a Ti/PANI nanocomposite can be used as a very good adsorbent to remove dyes in neutral media.

#### Funding

This research received no external funding.

#### Acknowledgments

This research has no acknowledgment.

## Conflicts of Interest

The authors declare no conflict of interest.

## References

1. Ramesh, T.N.; Kirana, D.V.; Ashwini, A.; Manasa, T.R. Calcium hydroxide as low-cost adsorbent for the effective removal of indigo carmine dye in water. *Journal of Saudi Chemical Society* **2017**, *21*, 165-171, <https://doi.org/10.1016/j.jscs.2015.03.001>.
2. Chen, J.; Hu, H.; Yang, J.; Xue, H.; Tian, Y.; Fan, K.; Zeng, Z.; Yang, J.; Wang, R.; Liu, Y. Removal behaviors and mechanisms for series of azo dye wastewater by novel nano constructed macro-architectures material. *Bioresour. Technol.* **2021**, *322*, 124556, <https://doi.org/10.1016/j.biortech.2020.124556>.
3. Muedas-Taípe, G.; Maza Mejía, I.M.; Santillan, F.A.; Velásquez, C.J.; Asencios, Y.J.O. Removal of azo dyes in aqueous solutions using magnetized and chemically modified chitosan beads. *Mater. Chem. Phys.* **2020**, *256*, 123595, <https://doi.org/10.1016/j.matchemphys.2020.123595>.
4. Shen, K.; Gondal, M.A. Removal of hazardous Rhodamine dye from water by adsorption onto exhausted coffee ground. *Journal of Saudi Chemical Society* **2017**, *21*, S120-S127, <https://doi.org/10.1016/j.jscs.2013.11.005>.
5. Sirajudheen, P.; Nikitha, M.R.; Karthikeyan, P.; Meenakshi, S. Perceptive removal of toxic azo dyes from water using magnetic Fe<sub>3</sub>O<sub>4</sub> reinforced graphene oxide-carboxymethyl cellulose recyclable composite: Adsorption investigation of parametric studies and their mechanisms. *Surfaces and Interfaces* **2020**, *21*, 100648, <https://doi.org/10.1016/j.surfin.2020.100648>.
6. Iervolino, G.; Vaiano, V.; Palma, V. Enhanced azo dye removal in aqueous solution by H<sub>2</sub>O<sub>2</sub> assisted non-thermal plasma technology. *Environmental Technology & Innovation* **2020**, *19*, 100969, <https://doi.org/10.1016/j.eti.2020.100969>.
7. Mais, L.; Vacca, A.; Mascia, M.; Usai, E.M.; Tronci, S.; Palmas, S. Experimental study on the optimisation of azo-dyes removal by photo-electrochemical oxidation with TiO<sub>2</sub> nanotubes. *Chemosphere* **2020**, *248*, 125938, <https://doi.org/10.1016/j.chemosphere.2020.125938>.
8. Sirajudheen, P.; Karthikeyan, P.; Basheer, M.C.; Meenakshi, S. Adsorptive removal of anionic azo dyes from effluent water using Zr(IV) encapsulated carboxymethyl cellulose-montmorillonite composite. *Environmental Chemistry and Ecotoxicology* **2020**, *2*, 73-82, <https://doi.org/10.1016/j.eneco.2020.04.002>.
9. Zafar, M.N.; Dar, Q.; Nawaz, F.; Zafar, M.N.; Iqbal, M.; Nazar, M.F. Effective adsorptive removal of azo dyes over spherical ZnO nanoparticles. *Journal of Materials Research and Technology* **2019**, *8*, 713-725, <https://doi.org/10.1016/j.jmrt.2018.06.002>.
10. Santos, S.S.G.; França, D.B.; Castellano, L.R.C.; Trigueiro, P.; Silva Filho, E.C.; Santos, I.M.G.; Fonseca, M.G. Novel modified bentonites applied to the removal of an anionic azo-dye from aqueous solution. *Colloids Surf. Physicochem. Eng. Aspects* **2020**, *585*, 124152, <https://doi.org/10.1016/j.colsurfa.2019.124152>.
11. Ali, F.; Ali, N.; Bibi, I.; Said, A.; Nawaz, S.; Ali, Z.; Salman, S.M.; Iqbal, H.M.N.; Bilal, M. Adsorption isotherm, kinetics and thermodynamic of acid blue and basic blue dyes onto activated charcoal. *Case Studies in Chemical and Environmental Engineering* **2020**, *2*, 100040, <https://doi.org/10.1016/j.csee.2020.100040>.
12. Orozco, R.S.; Martínez-Juan, M.; García-Sánchez, J.J.; Ureña-Núñez, F. Removal of methylene blue from aqueous solution using typha stems and leaves. *BioResources* **2018**, *13*, 1696-1710, <https://doi.org/10.15376/biores.13.1.1696-1710>.
13. Aliabadi, R.S.; Mahmoodi, N.O. Synthesis and characterization of polypyrrole, polyaniline nanoparticles and their nanocomposite for removal of azo dyes; sunset yellow and Congo red. *Journal of Cleaner Production* **2018**, *179*, 235-245, <https://doi.org/10.1016/j.jclepro.2018.01.035>.
14. Nicoara, A. I.; Ene, V. L.; Voicu, B. B.; Bucur, M. A.; Neacsu, I. A.; Vasile, B. S.; Iordache, F. Biocompatible Ag/Fe-Enhanced TiO<sub>2</sub> Nanoparticles as an Effective Compound in Sunscreens. *Nanomaterials*, **2020**, *10*, 570, <https://doi.org/10.3390/nano10030570>.
15. Zhao, W.; Liu, S.; Zhang, S.; Wang, R.; Wang, K. Preparation and visible-light photocatalytic activity of N-doped TiO<sub>2</sub> by plasma-assisted sol-gel method. *Catal. Today* **2019**, *337*, 37-43, <https://doi.org/10.1016/j.cattod.2019.04.024>.
16. Jang, I.; Leong, H.J.; Noh, H.; Kang, T.; Kong, S.; Oh, S.-G. Preparation of N-functionalized TiO<sub>2</sub> particles using one-step sol-gel method and their photocatalytic activity. *Journal of Industrial and Engineering Chemistry* **2016**, *37*, 380-389, <https://doi.org/10.1016/j.jiec.2016.04.002>.

17. Reddam, H.A.; Elmail, R.; Lloria, S.C.; Tomás, G.M.; Reddam, Z.A.; Coloma-Pascual, F. Synthesis of Fe, Mn and Cu modified TiO<sub>2</sub> photocatalysts for photodegradation of Orange II. *boletín de la sociedad española de cerámica y vidrio* **2020**, *59*, 138-148, <https://doi.org/10.1016/j.bsecv.2019.09.0050366-3175>.
18. De, A.; Boxi, S.S. Application of Cu impregnated TiO<sub>2</sub> as a heterogeneous nanocatalyst for the production of biodiesel from palm oil. *Fuel* **2020**, *265*, 117019, <https://doi.org/10.1016/j.fuel.2020.117019>.
19. Kharazi, P.; Rahimi, R.; Rabbani, M. Copper ferrite-polyaniline nanocomposite: Structural, thermal, magnetic and dye adsorption properties. *Solid State Sciences* **2019**, *93*, 95-100, <https://doi.org/10.1016/j.solidstatesciences.2019.05.007>.
20. Hashemi Monfared, A.; Jamshidi, M. Synthesis of polyaniline/titanium dioxide nanocomposite (PANI/TiO<sub>2</sub>) and its application as photocatalyst in acrylic pseudo paint for benzene removal under UV/VIS lights. *Prog. Org. Coat.* **2019**, *136*, 105257, <https://doi.org/10.1016/j.porgcoat.2019.105257>.
21. Ranjitha, A.; Thambidurai, M.; Shini, F.; Muthukumarasamy, N.; Velauthapillai, D. Effect of doped TiO<sub>2</sub> film as electron transport layer for inverted organic solar cell. *Materials Science for Energy Technologies* **2019**, *2*, 385-388, <https://doi.org/10.1016/j.mset.2019.02.006>.
22. Zhang, L.; Han, B.; Cheng, P.; Hu, Y.H. In-situ FTIR-DRS investigation on shallow trap state of Cu-doped TiO<sub>2</sub> photocatalyst. *Catal. Today* **2020**, *341*, 21-25, <https://doi.org/10.1016/j.cattod.2018.06.049>.
23. McManamon, C.; O'Connell, J.; Delaney, P.; Rasappa, S.; Holmes, J.D.; Morris, M.A. A facile route to synthesis of S-doped TiO<sub>2</sub> nanoparticles for photocatalytic activity. *J. Mol. Catal. A: Chem.* **2015**, *406*, 51-57, <https://doi.org/10.1016/j.molcata.2015.05.002>.
24. Ren, L.; Huang, X.; Sun, F.; He, X. Preparation and characterization of doped TiO<sub>2</sub> nanodandelion. *Mater. Lett.* **2007**, *61*, 427-431, <https://doi.org/10.1016/j.matlet.2006.04.097>.
25. Butoi, B.; Groza, A.; Dinca, P.; Balan, A.; Barna, V. Morphological and Structural Analysis of Polyaniline and Poly(o-anisidine) Layers Generated in a DC Glow Discharge Plasma by Using an Oblique Angle Electrode Deposition Configuration. *Polymers* **2017**, *9*, <https://doi.org/10.3390/polym9120732>.
26. Singh, R.; Choudhary, R.B. Ag/AgCl sensitized n-type ZnO and p-type PANI composite as an active layer for hybrid solar cell application. *Optik* **2021**, *225*, 165766, <https://doi.org/10.1016/j.ijleo.2020.165766>.
27. Bai, S.; Tian, Y.; Cui, M.; Sun, J.; Tian, Y.; Luo, R.; Chen, A.; Li, D. Polyaniline@SnO<sub>2</sub> heterojunction loading on flexible PET thin film for detection of NH<sub>3</sub> at room temperature. *Sensors Actuators B: Chem.* **2016**, *226*, 540-547, <https://doi.org/10.1016/j.snb.2015.12.007>.
28. Melánová, K.; Beneš, L.; Zima, V.; Trchová, M.; Stejskal, J. Polyaniline–zirconium phosphonate composites: Thermal stability and spectroscopic study. *J. Phys. Chem. Solids* **2020**, *147*, 109634, <https://doi.org/10.1016/j.jpcs.2020.109634>.
29. Khairy, M. Synthesis, characterization, magnetic and electrical properties of polyaniline/NiFe<sub>2</sub>O<sub>4</sub> nanocomposite. *Synth. Met.* **2014**, *189*, 34-41, <http://dx.doi.org/10.1016/j.synthmet.2013.12.022>.
30. Dascalu, I.; Culita, D.; Calderon-Moreno, J.M.; Osiceanu, P.; Hornoiu, C.; Anastasescu, M.; Somacescu, S.; Gartner, M. Structural, textural, surface chemistry and sensing properties of mesoporous Pr, Zn modified SnO<sub>2</sub>-TiO<sub>2</sub> powder composites. *Ceram. Int.* **2016**, *42*, 14992-14998, <https://doi.org/10.1016/j.ceramint.2016.06.146>.
31. Mandal, S.; Mahapatra, S.S.; Patel, R.K. Enhanced removal of Cr(VI) by cerium oxide polyaniline composite: Optimization and modeling approach using response surface methodology and artificial neural networks. *Journal of Environmental Chemical Engineering* **2015**, *3*, 870-885, <https://doi.org/10.1016/j.jece.2015.03.028>.
32. Zulfiqar, M.; Sufian, S.; Rabat, N.E.; Mansor, N. Photocatalytic degradation and adsorption of phenol by solvent-controlled TiO<sub>2</sub> nanosheets assisted with H<sub>2</sub>O<sub>2</sub> and FeCl<sub>3</sub>: Kinetic, isotherm and thermodynamic analysis. *J. Mol. Liq.* **2020**, *308*, 112941, <https://doi.org/10.1016/j.molliq.2020.112941>.
33. Zulfiqar, M.; Lee, S.Y.; Mafize, A.A.; Kahar, N.A.; Johari, K.; Rabat, N.E. Efficient Removal of Pb(II) from Aqueous Solutions by Using Oil Palm Bio-Waste/MWCNTs Reinforced PVA Hydrogel Composites: Kinetic, Isotherm and Thermodynamic Modeling. *Polymers* **2020**, *12*, <https://doi.org/10.3390/polym12020430>.
34. Zhang, H.; Tang, Y.; Cai, D.; Liu, X.; Wang, X.; Huang, Q.; Yu, Z. Hexavalent chromium removal from aqueous solution by algal bloom residue derived activated carbon: Equilibrium and kinetic studies. *J. Hazard. Mater.* **2010**, *181*, 801-808, <https://doi.org/10.1016/j.jhazmat.2010.05.084>.
35. Shah, B.A.; Shah, A.V.; Navik, A.J. Microwave-promoted M-PFR resin: kinetics, isotherms and sequestration of Cr(III) and Pb(II) from environmental samples. *Iranian Polymer Journal* **2012**, *21*, 569-582, <https://doi.org/10.1007/s13726-012-0061-y>.



36. Shah, A.; Khuhawar, M.Y.; Shah, A.A. Evaluation of sorption behavior of polymethylene-bis(2-hydroxybenzaldehyde) for Cu(II), Ni(II), Fe(III), Co(II) and Cd(II) ions. *Iranian Polymer Journal* **2012**, *21*, 325-334, <https://doi.org/10.1007/s13726-012-0033-2>.
37. Ho, Y. S.; Ng, J.C.Y.; McKay, G. Kinetics of Pollutant Sorption by Biosorbents: Review. *Sep. Purif. Methods* **2000**, *29*, 189-232, <https://doi.org/10.1081/SPM-100100009>.
38. Tsai, C.-G.; Tseng, W.J. Preparation of TiN–TiO<sub>2</sub> composite nanoparticles for organic dye adsorption and photocatalysis. *Ceram. Int.* **2020**, *46*, 14529-14535, <https://doi.org/10.1016/j.ceramint.2020.02.252>.
39. Saad, M.; Tahir, H.; Khan, J.; Hameed, U.; Saud, A. Synthesis of polyaniline nanoparticles and their application for the removal of Crystal Violet dye by ultrasonicated adsorption process based on Response Surface Methodology. *Ultrason. Sonochem.* **2017**, *34*, 600-608, <https://doi.org/10.1016/j.ultrsonch.2016.06.022>.
40. Srivastava, V.; Sharma, Y.C.; Sillanpää, M. Response surface methodological approach for the optimization of adsorption process in the removal of Cr(VI) ions by Cu<sub>2</sub>(OH)<sub>2</sub>CO<sub>3</sub> nanoparticles. *Appl. Surf. Sci.* **2015**, *326*, 257-270, <https://doi.org/10.1016/j.apsusc.2014.11.097>.
41. Baghdadi, M. UT (University of Tehran) isotherm as a novel and useful adsorption isotherm for investigation of adsorptive removal of pollutants. *Journal of Environmental Chemical Engineering* **2017**, *5*, 1906-1919, <https://doi.org/10.1016/j.jece.2017.03.037>.
42. Inyang, H.I.; Onwawoma, A.; Bae, S. The Elovich equation as a predictor of lead and cadmium sorption rates on contaminant barrier minerals. *Soil and Tillage Research* **2016**, *155*, 124-132, <https://doi.org/10.1016/j.still.2015.07.013>.
43. Mondal, S.; Majumder, S.K. Honeycomb-like porous activated carbon for efficient copper (II) adsorption synthesized from natural source: Kinetic study and equilibrium isotherm analysis. *Journal of Environmental Chemical Engineering* **2019**, *7*, 103236, <https://doi.org/10.1016/j.jece.2019.103236>.
44. Uslu, H.; Majumder, S. Adsorption Studies of Lactic Acid by Polymeric Adsorbent Amberlite XAD-7: Equilibrium and Kinetics. *J. Chem. Eng. Data* **2017**, *62*, 1501-1506, <https://doi.org/10.1021/acs.jced.6b01062>.
45. Zhang, H.; Wang, Y.; Bai, P.; Guo, X.; Ni, X. Adsorptive Separation of Acetic Acid from Dilute Aqueous Solutions: Adsorption Kinetic, Isotherms, and Thermodynamic Studies. *J. Chem. Eng. Data* **2016**, *61*, 213-219, <https://doi.org/10.1021/acs.jced.5b00481>.